Semiconductor Fano Lasers

Jesper Mork, Yi Yu, Thorsten S. Rasmussen, Elizaveta Semenova, and Kresten Yvind

(Invited Paper)

***Abstract*—In this paper, a new type of semiconductor laser based on Fano interference is described. One of the laser mirrors relies on the interference between the continuum of waveguide modes and a side-coupled nanocavity, leading to a narrow-band mirror that provides the Fano laser with unique characteristics. In addition to being truly single-mode, the laser can be modulated through the mirror at frequencies far exceeding the relaxation oscillation resonance. Furthermore, nonlinearities in the nanocavity can be used to implement a saturable mirror, leading to passive pulse generation with repetition frequencies in the gigahertz range. This paper reviews the theory of Fano lasers and the current experimental status. Experimentally, the Fano laser concept is demonstrated using a photonic crystal platform with quantum dot active material. Both continuous wave operation and self-pulsing is observed for optically pumped lasers operating at room temperature.**

***Index Terms*—Semiconductor lasers, nanotechnology, optical pulse generation, photonic bandgap materials.**

I. Introduction

SEMICONDUCTOR lasers are key enabling devices for the internet as they facilitate conversion of data in electronic form to optical signals that can be transmitted over long distances in optical fibers. Compact lasers continue to find new applications, e.g., within optical sensing and spectroscopy, biomedical applications, and lighting. As always, there is a push towards making lasers smaller and more energy efficient. This is particularly important for applications within the developing area of silicon photonics, where lasers are integrated on the same chip as CPUs and used to power high-speed and ultra-low-power optical interconnects between or within chips [1].

Since its invention in 1962, the semiconductor laser has undergone a spectacular development enabled by new possibilities for nanofabrication and novel ideas for realizing high quality optical cavities and advanced gain materials, the two main ingredients of any laser. Fig. 1 shows an overview of different types of laser cavities [2], including (a) the Fabry-Pérot laser, (b) the Distributed Bragg Reflector (DBR) laser, which is closely related to the Vertical-Cavity Surface Emitting Laser (VCSEL), and (c) the Distributed-Feedback (DFB) laser. These lasers all play important roles in various applications and also exist in more advanced versions, e.g., involving multiple sections for realizing wavelength tuning or short-pulse generation [2]. Further, Fig. 1 illustrates (d) a photonic crystal cavity laser [3]–[5], (e) a whispering gallery mode cavity [6], and (f) a random cavity laser [7]. These laser cavities all rely on reflections at interfaces between materials with different refractive indices. In cases (b), (c), and (d) interference effects between multiple reflections lead to spatially distributed reflectivities.

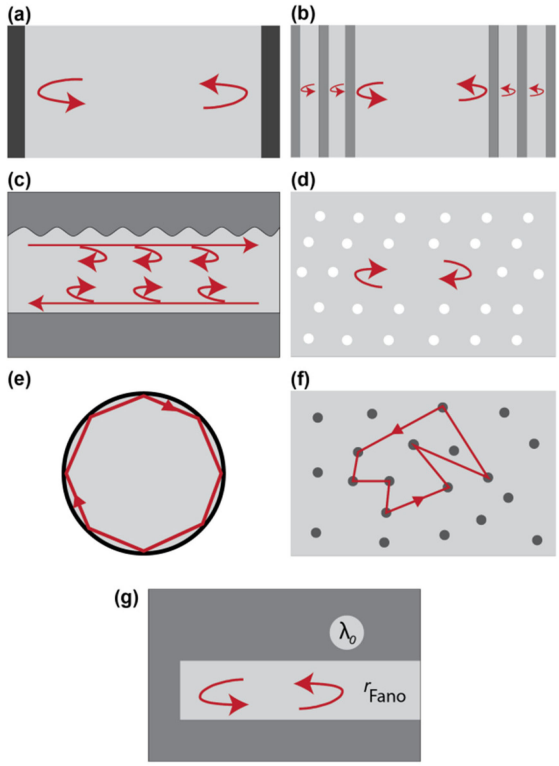

Fig. 1. Different types of laser cavities: (a) Fabry-Pérot laser; (b) Distributed-Bragg-Reflector laser; (c) Distributed-Feedback Laser; (d) Photonic crystal line-defect laser; (e) Whispering-Gallery-Mode laser; (f) Random laser; (g) Fano laser.

In this paper we review and discuss the properties of a new type of laser structure, a so-called Fano laser, illustrated in Fig. 1(g), where one (or both) of the laser mirrors is realized using Fano interference. In Fig. 1(g) the reflectivity of the right mirror thus occurs due to interference between the continuum of waveguide modes and a single discrete mode of the cavity that is side-coupled to the waveguide. This gives rise to a mirror reflectivity that is highly dispersive and equips the laser with a

Manuscript received February 19, 2019; revised May 28, 2019; accepted June 1, 2019. Date of publication June 11, 2019; date of current version July 11, 2019. This work was supported by the Villum Foundation through the NATEC Centre of Excellence under Grant 8692. *(Corresponding author: Jesper Mork.)*

The authors are with DTU Fotonik, Department of Photonics Engineering, Technical University of Denmark, DK-2800 Lyngby, Denmark (e-mail: jesm@fotonik.dtu.dk; yiyu@fotonik.dtu.dk; thsv@fotonik.dtu.dk; esem@fotonik.dtu.dk; kryv@fotonik.dtu.dk).

Color versions of one or more of the figures in this paper are available online at http://ieeexplore.ieee.org.

Digital Object Identifier 10.1109/JSTQE.2019.2922067

number of unique properties. The Fano laser was suggested and theoretically analyzed in [8] and experimentally demonstrated in [9].

The Fano interference is a general wave phenomenon and has been observed in many different physical systems, including quantum mechanics, acoustics, plasmonics and optics [10]–[12]. The interferometric nature of the resonance gives rise to a strong wavelength dependence of the amplitude as well as the phase of the Fano mirror reflectivity, leading to novel laser characteristics. In particular, since the mirror reflectivity depends on the resonance frequency of the side-coupled cavity, the laser may be modulated via the mirror, either via direct external modulation, be it electrical or optical, or due to self-modulation, mediated by nonlinearities in the side-coupled cavity. It was predicted that Fano lasers can be modulated at frequencies far exceeding the relaxation resonance frequency [8], which limits the bandwidth of conventional semiconductor lasers [2]. Furthermore the strong dispersion of the Fano mirror in combination with optical nonlinearities means that the system has very rich dynamics, e.g., resulting in the first observation of passive short-pulse generation in nanolasers [9].

The modal properties of the Fano laser differ drastically from conventional lasers, and rather relate to the characteristics of a new class of modes, denoted as "bound-modes in the continuum" [13]. A laser based on such a mode was recently demonstrated experimentally [14]. In such lasers, the mere existence of the lasing mode depends very sensitively on external parameters [15], which is also the case for the Fano laser.

In this paper we review the theory of Fano lasers, present the experimental status, and outline future directions of research. The theoretical and experimental investigations of the Fano laser have so far been based on a photonic crystal membrane structure [16]. This platform has proven its strength by allowing the experimental realization of the semiconductor laser with the lowest threshold current demonstrated so far [5]. Laser integration on a silicon photonic chip has also been demonstrated [17]. However, the Fano laser concept is not limited to the photonic crystal platform. The main requirement for realizing this laser type is that the cavity that is side-coupled to the laser waveguide to form the Fano interference must be of the standing-wave type. Thus, a microring [18] cannot be employed, since it does not provide the momentum needed for back-scattering photons into the laser waveguide.

The waveguide-nanocavity Fano resonance can also be used to implement optical signal processing [19]–[24], in which case one exploits the sharp spectral features of the Fano resonance to lower the energy consumption or increase the switching contrast.

It also needs to be mentioned that Fano resonances in photonic crystal membranes or slabs can be explored in another geometry, where the incoming light-beam is perpendicular to the slab and involves guided resonances of the slab [25]. In the context of lasers, this geometry can be used to realize broadband reflectors, and is closely related to the topic of so-called high-contrast grating mirrors and lasers [26], which using special geometries can emit into on-chip waveguides [27]. In this paper we shall limit consideration to the in-plane geometry.

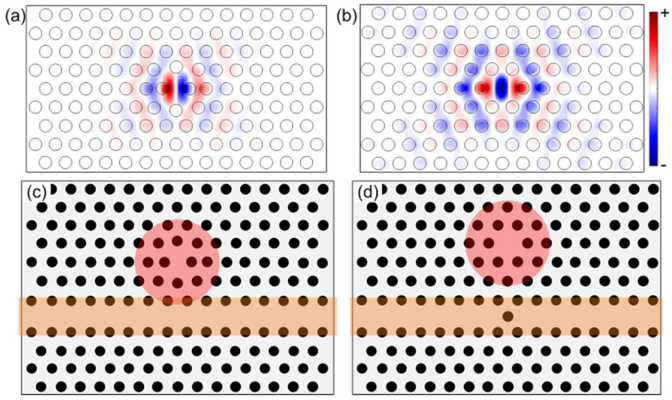

Fig. 2. (a, b) Field pattern (transverse E_y component, colour scale) of the resonant mode of an (a) H0 and (b) H1 photonic crystal point-defect cavity, as calculated using the finite-difference time-domain (FDTD) technique. Black circles are airholes in a semiconductor membrane. Corresponding cavity-waveguide structures are shown in (c) and (d), with (d) showing an example where an airhole is placed in the waveguide below the nanocavity to act as a partially transmitting element (PTE).

The paper is organized as follows: In Section II we explain the origin of Fano resonances in the context of a waveguide coupled to a cavity and its use for realizing a laser. Section III develops the theory for semiconductor Fano lasers, starting with the basic oscillation condition determining the mode of the laser and then proceeding to a dynamical model for the laser. Based on this model, the topics of self-pulsing and ultrafast modulation are discussed. In Section IV we explain the principle used to design Fano lasers and the actual fabrication process. Section V presents key experimental results and finally Section VI summarizes the results and discusses future research opportunities for Fano lasers.

II. Fano Laser Principle

The type of resonance that we today denote by "Fano Resonance" was first described by Ugo Fano in the context of explaining in-elastic scattering of electrons by Helium [28]. We refer to [10], [11] for excellent reviews of Fano resonances in the context of optics and plasmonics. Here we explain how Fano resonances appear in waveguides that are coupled to nanocavities [29], which is the configuration used in Fano lasers.

A. Waveguides and Cavities in Photonic Crystals

By using the concept of photonic crystals, light propagation can be effectively controlled in semiconductor membranes [30]. Fig. 2 shows an example of a point-defect nanocavity (red-shaded region) which is side-coupled to a line-defect waveguide (orange-shaded). The black circles indicate airholes in a semiconductor membrane with a thickness of the order of 300 nm. The radius and period of the honeycomb lattice of airholes are chosen such as to achieve an in-plane bandgap covering the range of wavelengths within which waveguides and cavities are to be realized. Transverse confinement is due to total internal reflection in the membrane.

For example, a point defect nanocavity can be simply created by omitting a single airhole (H1-type) [31] in an otherwise periodic photonic crystal lattice or by shifting two neighboring holes in opposite directions (H0-type) [32], [33]. This leads to spatially localized modes with ultra-small effective mode volume comparable to or even smaller than the diffraction-limited value of $(\lambda/2n)^3$. In this context, we notice that new designs involving bow-tie like geometries may lead to mode volumes significantly below the diffraction limit [34]–[36].

B. Fano Resonance

We now calculate the reflection coefficient experienced by an optical signal propagating in the waveguide of Fig. 2(a) due to the interaction with the side-coupled nanocavity. This configuration can be easily modelled using coupled-mode theory [29], [37]. It was shown that the inclusion of a blocking airhole in the waveguide below the nanocavity (denoted by PTE, partially transmitting element, in Fig. 2(a)) can be used to vary the amplitude of the continuum-path of the Fano resonance via the airhole radius, thereby controlling the shape of the Fano resonance [20]. Including this effect we arrive at the following expression for the intensity transmission coefficient, *T*, through the waveguide section containing the nanocavity and the PTE (if present) [20]

$$|T(\omega)|^2 = \left| -it_B + (it_B \pm r_B)\,\frac{\gamma_c}{i(\omega_c - \omega) + \gamma_T} \right|^2. \qquad (1)$$

The sign $\pm$ is determined by the symmetry of the nanocavity mode, i.e., whether the mode is odd $(+)$ or even $(-)$ with respect to the cavity symmetry line. Eq. (1) assumes that the PTE is placed in the symmetry line of the nanocavity which then couples equally to left-going and right-going waveguide modes; a more general expression may be found in [38]. Here, ω_c is the resonance frequency of the relevant mode of the nanocavity, γ_c is the (field) coupling rate from that mode of the nanocavity to the waveguide and γ_T is the total decay rate of the nanocavity, including coupling to the waveguide, out-of plane diffraction losses and coupling to other ports, if present. Both γ_c and $\gamma_T$will be affected by the presence of an air-hole in the waveguide but are, as defined here, independent of other reflectors in the waveguide. The total quality factor of the nanocavity is given by $Q_T = \omega_c/(2\gamma_T)$, and in general we define $Q_x = \omega_c/(2\gamma_x)$. In (1), r_B is the (real) amplitude reflection coefficient of the PTE below the nanocavity and $t_B^2 = 1 - r_B^2$ is the corresponding amplitude transmission coefficient.

In the absence of an air-hole, $t_B = 1$, Eq. (1) shows that there is a dip in the transmission through the waveguide at the resonance frequency of the nanocavity due to destructive interference between the direct waveguide path and the indirect waveguide-cavity-waveguide path. The dip in transmission corresponds to the presence of a back-scattered field. This is the essence of the waveguide-cavity Fano interference and its use for realizing a (Fano) mirror with narrowband reflection. The frequency dependence of the transmission or reflection coefficient depends on the relative amplitude of the two paths, and can be controlled via the PTE [20], as also demonstrated experimentally [21]. Due to other decay paths of the nanocavity field besides coupling to the waveguide, the reflectivity of the Fano mirror is not simply given by $1 - |T|^2$. From coupled mode theory one derives the expression

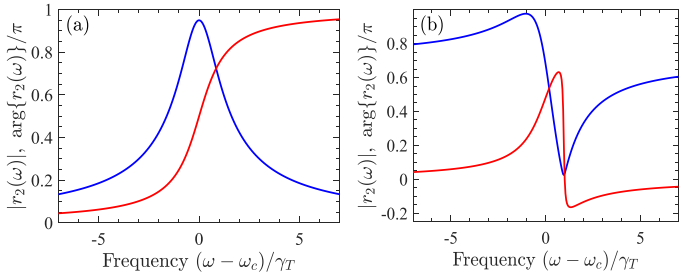

Fig. 3. Calculated reflection amplitude (blue) and reflection phase (red) for a nanocavity side-coupled to a waveguide. (a) Absence of blocking airhole in the waveguide ($r_B = 0$) and (b) presence of blocking airhole ($r_B = 1/\sqrt{2}$) in the case of coupling to an even mode of the nanocavity. The ratio of the total quality factor of the nanocavity to the coupling Q is $Q_T/Q_c = 0.95$ in both cases.

$$r_2 = r_B + (\mp it_B - r_B)\,\frac{\gamma_c}{i(\omega_c - \omega) + \gamma_T} \qquad (2)$$

Here, the $-$ $(+)$ sign corresponds to an odd (even) nanocavity mode. Fig. 3 shows examples of the calculated frequency dependence of the amplitude and phase of the Fano mirror reflectivity for two different values of the PTE reflectivity.

In the absence of a PTE, Fig. 3(a) for $r_B = 0$, the reflection curve is symmetric and peaks at the resonance frequency of the nanocavity. At that frequency, the field coupled from the nanocavity to the waveguide interferes destructively with the field in the waveguide, leading to a drastic reduction in the amplitude of the field that passes the region containing the nanocavity and a corresponding increase in the reflectivity.

In the presence of the PTE, Fig. 3(b) for $r_B = 1/\sqrt{2}$, the amplitudes of the two paths differ at the resonance of the nanocavity and the peak reflectivity is achieved at a frequency that is slightly offset with respect to the nanocavity resonance. On the other hand, the finite reflectivity of the PTE also implies that there is a frequency where the two paths are nearly in phase and have similar amplitudes, leading to an enhancement of the transmission within the resonance bandwidth and a corresponding dip in the reflectivity.

One often defines a Fano asymmetry parameter, q [10], with $q = 0$ corresponding to a symmetric Fano resonance profile and $q<0$ or $q>0$, corresponding to asymmetric profiles with different parity [39], i.e., signifying whether the reflectivity minimum is blue-shifted or red-shifted with respect to the maximum. It has been shown theoretically [39] and experimentally [38] that the parity of the waveguide-cavity geometry can be controlled by displacing the PTE with respect to the symmetry line through the nanocavity.

Asymmetric Fano resonances have been shown to be advantageous for implementing all-optical switching [40], [41], signal re-shaping and pulse carving [42] as well as non-reciprocal transmission [38]. Compared to their symmetric (Lorentzian) counterpart, an asymmetric Fano structure can achieve higher

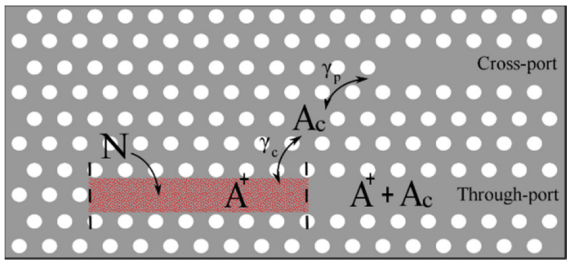

Fig. 4. Schematic of Fano laser implemented in a photonic crystal membrane. The red-hatched area is the laser cavity, where gain is provided by active material. The left mirror is a conventional photonic crystal mirror, reflecting that the laser wavelength is located within the bandgap of the surrounding photonic crystal structure. The right mirror is a Fano mirror occuring due to interference between the right-propagating field, A^+, in the laser cavity and the field, A_c, in the side-coupled nanocavity. Two in-plane output ports for the laser are shown, i.e., the through-port and the cross-port.

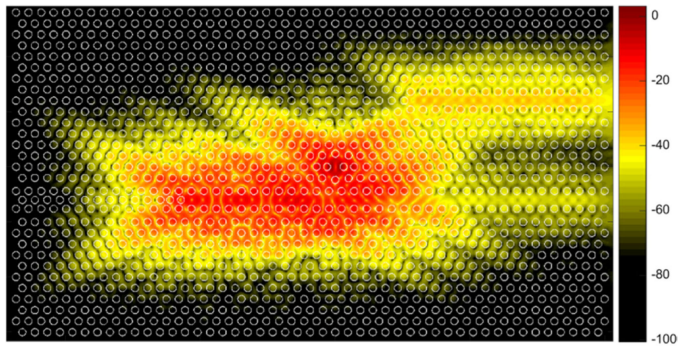

Fig. 5. Example FDTD simulation of field distribution ($|E|$) in Fano laser. The color-scale is logarithmic (dB).

on-off ratio for the same resonance shift due to the close spectral location of the transmission maximum and minimum.

In the absence of a PTE, $r_B = 0$, the maximum Fano mirror reflectivity becomes

$$|r_{2,\max}| = 1 - \frac{Q_T}{Q_i} = \frac{Q_T}{Q_c}, \tag{3}$$

where Q_i is the intrinsic quality factor of the nanocavity in the absence of coupling to the waveguide, with $Q_T^{-1} = Q_c^{-1} + Q_i^{-1}$. The maximum reflectivity approaches unity when the total loss of the nanocavity is dominated by coupling to the waveguide, corresponding to $Q_i \gg Q_T$. The finite value of Q_i is mainly governed by vertical coupling due to diffraction losses and residual absorption in the membrane. It was shown that nanocavities with intrinsic Q-factors exceeding 9 million can be achieved by careful cavity design and material treatment [43]. Since the nanocavity can be strongly coupled to the waveguide, achieving coupling quality factors of the order of a few hundred, it is quite easy to achieve a high Fano mirror reflectivity, even in the presence of a moderate value for the intrinsic Q_i.

C. Fano Laser Configuration

A schematic of the Fano laser including important parameters is shown in Fig. 4. We denote the region between the left mirror and the Fano mirror as "laser cavity" in order to separate it from the nanocavity. The laser output can be provided directly via the waveguide, denoted as the through-port, but we have also included a so-called cross-port, obtained by coupling another waveguide to the nanocavity. It was shown in [8] that the quantum efficiency for out-coupling through the cross-port strongly exceeds that of the through-port, due to the very high reflectivity of the Fano mirror as well as the fact that the intensity in the nanocavity largely exceeds that of the laser cavity during lasing. Notice that the addition of the cross-port lowers the intrinsic quality factor, Q_i, discussed in connection with Eq. (3).

Fig. 5 illustrates the field distribution in the Fano laser under conditions of lasing, as obtained by finite-difference time-domain (FDTD) simulation for an effective 2D structure. The cross-port shown in Fig. 4 is included and it is seen that the field in this port strongly exceeds that of the through-port. Furthermore, the largest field strength is obtained in the nanocavity.

III. Fano Laser Theory

In this section we present a theoretical model of the Fano laser as developed in [8], [9], [44]. Many of the features of the Fano laser that distinguish it from conventional laser geometries can be appreciated by considering the steady-state oscillation condition and the tuning characteristics of the laser. Subsequently we develop a dynamical model for the laser and analyze different regimes of operation. Finally, the possibility of dynamically modulating the laser at ultra-high frequencies is analyzed.

A. Oscillation Condition and Tuning Characteristics

In general, the oscillation condition for a laser may be expressed

$$r_1(\omega) r_2(\omega) \exp[2ik(\omega, N)L] = 1, \tag{4}$$

where ω is the laser oscillation frequency, r_1 and r_2 are the left and right field reflectivities of the laser cavity, L is the cavity length and k is the complex wave number

$$k(\omega, N) = \frac{\omega}{c} n(\omega, N) - i\frac{1}{2}[\Gamma g(\omega, N) - \alpha_i]. \tag{5}$$

Here, N is the carrier density in the laser cavity (see Fig. 4), n is the refractive index, Γ is the confinement factor, g is the material gain and α_i is the internal waveguide loss. For a Fabry-Pérot laser, r_1 and r_2 can be taken as frequency independent. In contrast, for the Fano laser, the amplitude as well as the phase of r_2 is given by (2) and depends strongly on frequency, as shown in Fig. 3. If the left mirror of the Fano laser is implemented as a photonic bandgap mirror, as shown in Fig. 4, r_1 can be approximated as frequency independent in the range of interest [45]. However, one can also base the Fano laser on two Fano mirrors, in which case both laser mirrors are highly dispersive.

By invoking linear expansions of the gain and refractive index and separately considering the argument and the norm, Eq. (4) leads to phase and amplitude conditions that determine the oscillation frequency, $\omega = \omega_s$, and the required threshold gain $g = g_{th} = g_N(N_s - N_0)$ [44]. Here, N_s is the steady-state

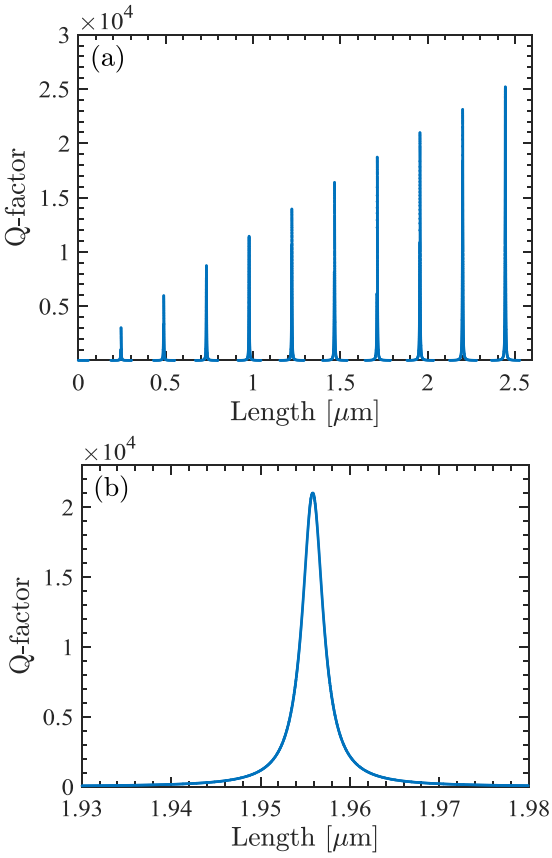

Fig. 6. Variation of quality factor with mirror separation for passive Fano laser cavity. (a) Large-scale variation and (b) zoom-in of variation close to one of the resonances. For these simulations we used $Q_T = 500$, $Q_i = 100000$ and assumed $\alpha = 0$.

value of the active region carrier density and g_N and N_0 are the differential gain and transparency carrier density in a linear expansion of the gain neglecting the frequency dependence. The latter is a very good approximation, considering the strong frequency dependence of the Fano mirror reflectivity.

If the oscillation frequency of the laser is known, the amplitude condition gives the threshold gain and thereby the photon lifetime and quality factor Q of the Fano laser cavity

$$\Gamma v_g g_{th} = \frac{1}{\tau_p} = \frac{\omega_s}{Q} = v_g \left[\alpha_i + \frac{1}{L} \ln \left(\frac{1}{|r_1|\,|r_2(\omega_s)|} \right) \right], \quad (6)$$

where v_g is the group velocity. If one neglects the carrier density dependence of the refractive index in (5), corresponding to the linewidth enhancement factor α [2] being zero, the phase condition can easily be solved for the cavity length L required for a laser to oscillate at a given frequency $\omega = \omega_s$ and by insertion in (6) one finds the corresponding quality factor Q.

Fig. 6 shows an example of the calculated variation of the Q-factor for a Fano laser cavity in the case of $\alpha = 0$. It is seen that a high quality factor only is achieved at distinct values of the cavity length. For these cavity lengths, a longitudinal Fabry-Pérot mode of the laser cavity coincides with the resonance frequency of the nanocavity so that the Fano mirror reflectivity r_2 approaches unity. As the zoom-in of Fig. 6(b) shows, the quality factor drops to nearly half the peak value if the cavity length is changed less than 10 nm. The reason for this sensitive dependence of the cavity quality factor on the cavity length, which is not found for other lasers with dispersive mirrors such as DFB lasers or VCSELs, is of course the strong variation of the Fano mirror reflectivity with wavelength. For a smaller peak value of Q, the length dependence is less severe. Based on the analysis in [46] one may derive the following approximate expression for the length change ΔL that leads to a 3 dB decrease of the quality factor

$$\frac{\Delta L}{\lambda} \cong \frac{1}{4\pi n} \sqrt{\frac{\tau_{in}\omega_s}{Q}}, \quad (7)$$

where τ_{in} is the roundtrip time in the laser cavity. It is seen that the length dependence is not determined by the quality factor Q_T of the nanocavity, but rather by the laser cavity quality factor Q.

Ref. [47] considers the case of a photonic crystal laser containing two coupled cavities. It should be emphasized that the modes of the Fano laser qualitatively differ from such coupled-cavity structures. Thus, in the case where the side-coupled nanocavity is removed (and in the absence of a PTE), the laser cavity is open and does not support any discrete mode. Rather, modes of the laser cavity are only established due to coupling with the nanocavity. In this sense, the mode should rather be characterized as an example of a bound mode in the continuum [13], which has the characteristic feature of only existing in a narrow parameter range [15]. If one instead considers the localized mode of the nanocavity, rather than the laser cavity mode, it will have its maximum Q-value in the absence of coupling to the waveguide. Coupling to the waveguide will lower this Q, but the intrinsic Q-value of the nanocavity can be restored by adding a reflector in the waveguide and ensuring that the back-coupled field interacts destructively with the field coupled from the nanocavity [48]. This effect was used to demonstrate ultrafast dynamical control of the nanocavity Q-factor [48].

Fig. 7 shows the calculated variation of the threshold gain and laser oscillation frequency when the resonance frequency of the nanocavity is tuned and one takes into account the effect of a finite value for the alpha-parameter. Parameter values are given in Table I unless specified. Zero detuning corresponds to the case where the nanocavity resonance frequency matches with the roundtrip phase condition for the linear cavity, so as to yield a maximum of the quality factor for the lasing mode, cf. Fig. 6, and a minimum threshold gain. The periodicity seen in Fig. 7(a) reflects different longitudinal mode numbers. The asymmetry of the curves is due to the finite value of the alpha-parameter and the discontinuities observed at negative detunings reflect mode-jumps. Due to the large variation in threshold gain, the laser will only be able to lase in a rather narrow detuning range around the minimum. The corresponding variation in laser oscillation frequency ω_L, Fig. 7(b), shows that the Fano laser frequency nearly tracks the change in resonance frequency, with an off-set given by cavity loading [8], [46]. Thus, when the nanocavity resonance frequency is changed, the Fano laser needs to operate slightly off the Fano mirror peak in order to maintain the phase oscillation condition.

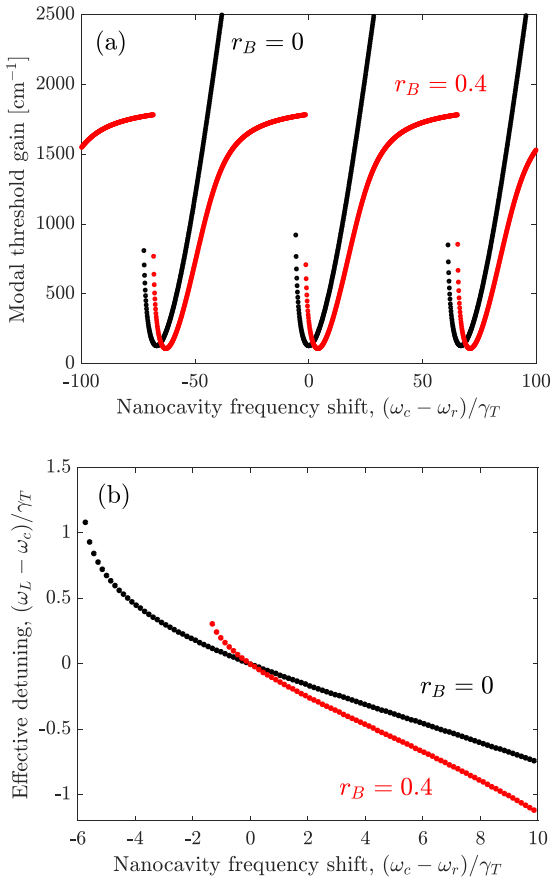

Fig. 7. Variation of (a) laser threshold gain and (b) oscillation frequency when the resonance frequency of the nanocavity is tuned in the absence of a PTE ($r_B = 0$, black curves) and in the presence of a PTE ($r_B = 0.4$, red curves). The case of zero nanocavity frequency shift corresponds to the laser oscillation frequency being equal to the nanocavity resonance frequency and this reference frequency is denoted ω_r.

TABLE I
PARAMETER VALUES USED IN SIMULATIONS OF THE FANO LASER UNLESS OTHERWISE SPECIFIED

Parameter	Symbol	Value
Reference wavelength	λ_r	1554 nm
Cavity-waveguide Q	Q_c	780
Vertical scattering Q	Q_v	100000
Cavity-third port Q	Q_p	15000
Internal loss	α_i	10 cm^{-1}
Left mirror reflectivity	r_1	-1
Phase and group indices	n, n_g	3.5
Linewidth enhancement factor	α	1
Waveguide confinement factor	Γ	0.01
Nanocavity confinement factor	Γ_C	0.01
Differential gain	g_N	5×10^{-16}m^{-2}
Transparency carrier density	N_0	5×10^{21}m^{-3}
Reference length	L_r	4.883 μm
Transverse area	A	0.20 μm^2
Carrier lifetimes	τ_s, τ_C	0.28 ns
Nanocavity volume	V_{NC}	1.6×10^{-19}m^3

B. Dynamical Model and Steady-State Characteristics

Based on the oscillation condition, Eq. (4), one can derive an evolution equation for the field in the laser cavity, denoted $A^+(t)$. This is accomplished using the method described in [49], where the oscillation condition is Taylor expanded in frequency around a steady-state solution (ω_s, N_s). By Fourier transforming the result, an ordinary differential equation describing the time evolution of the slowly-varying envelope field at a reference plane just left of the symmetry line of the nanocavity is obtained [8]. In order to dynamically model the Fano interference, one needs to also account for the field in the side-coupled nanocavity, $A_c(t)$, which can be done using the previously described coupled-mode theory by considering the right-propagating laser cavity field as the incoming field in the waveguide. Finally, these equations are complemented by a conventional rate equation for the free carrier density in the waveguide, $N(t)$, governing the gain in the laser cavity. The details of the derivation are given in [8], [9] with the final result being the following set of dynamical equations:

$$\frac{d}{dt}A^+(t) = \frac{1}{2}(1 - i\alpha)\left(\Gamma v_g g_N (N - N_0) - \frac{1}{\tau_p}\right)A^+(t) + \gamma_L\left(\frac{r_B A^+(t) + \sqrt{\gamma_c}A_c(t)}{r_2(\omega_s)} - A^+(t)\right) \quad (8)$$

$$\frac{d}{dt}A_c(t) = (-i\Delta\omega - \gamma_T)A_c(t) + e^{i2\theta_1}\sqrt{\gamma_c}A^+(t) \quad (9)$$

$$\frac{d}{dt}N = R_p - \frac{N}{\tau_s} - \frac{\Gamma}{V_{LC}}v_g g_N (N - N_0) \times \sigma(\omega_L, \omega_C)|A^+(t)|^2 \quad (10)$$

Here, $\gamma_L = 1/\tau_{in}$ is the inverse of the roundtrip time in the laser cavity, θ_1 is the coupling phase from waveguide to nanocavity, R_p is the carrier generation rate (representing electrical or optical pumping) and the carrier recombination rate $R(N) = N/\tau_s$ is described using a lifetime approximation, where τ_s is an effective lifetime. $\sigma(\omega_L, \omega_c)$ is a parameter relating the field strength and photon number through the relation $N_p = \sigma(\omega_L, \omega_c)|A^+(t)|^2$ [49] and V_{LC} is the active region volume. It should be noted that since these equations are based on an expansion near a steady-state solution, the frequency dependent parameters should take on the value corresponding to the steady-state solution. These are $\tau_p, r_2(\omega_L, \omega_c)$, $\Delta\omega$, and $\sigma(\omega_L, \omega_c)$.

In the case of the active material extending to the nanocavity, the equations above must be extended to account for linear absorption and carrier generation in the nanocavity. These effects can be incorporated by going back to the CMT description of the Fano reflection and adding a phenomenological absorption term to the equation for the nanocavity field, yielding an additional (saturable) reduction of the Fano mirror reflectivity. By modifying the expansion point appropriately and adding an additional rate equation for the carrier density in the nanocavity, the dynamical model can be extended in a rather straightforward manner to describe this case, see [9], [44] for details. In addition to linear absorption, nonlinear effects due to two-photon absorption and Kerr effects become important for high peak intensities

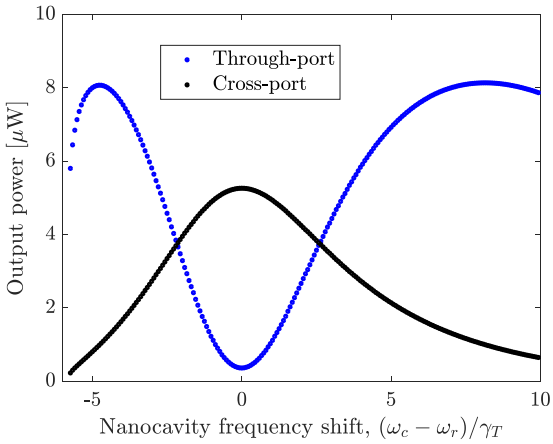

Fig. 8. Variation of output power in cross-port and through-port versus nanocavity resonance frequency for $r_B = 0$. The reference frequency ω_r is chosen such as to correspond to the minimum threshold gain.

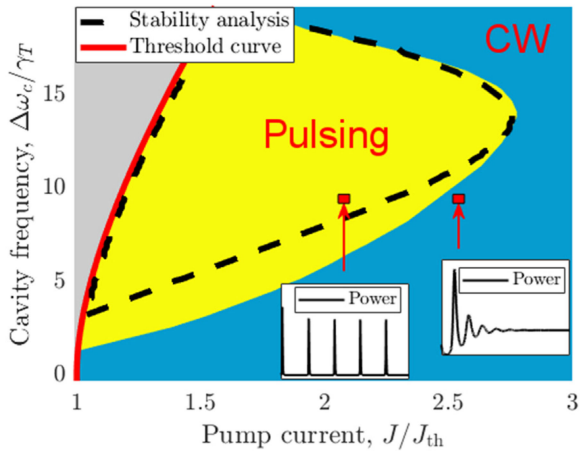

Fig. 9. Phase diagram of laser output as function of pump current and nanocavity frequency, Current is normalised to the minimum threshold current and detuning is normalized to the coupling rate γ_T. In the gray region the laser is below threshold (the laser threshold curve is shown in red), in the blue region the output is continuous-wave, and the region of self-pulsing is shown in yellow. The dashed black line shows the boundary of the self-pulsing regime predicted by a stability analysis. Insets show examples of the temporal variation of the laser intensity in different regions.

in the nanocavity. Such effects are used for all-optical switching in coupled waveguide-cavity structures [21], [33], [40], [50], [51], but appear not to be important for the regimes of operation investigated in this paper.

Coupled-mode theory gives the output field in the through-port, and cross-port [9], as

$$A_t(t) = e^{i(\theta_2-\theta_1)}\sqrt{\gamma_c}A_c(t) - it_B A^+(t) \tag{11}$$

$$A_x(t) = i\sqrt{\gamma_p}A_c(t), \tag{12}$$

where θ_i are the phases for the complex waveguide-nanocavity coupling coefficients from left and right. Here one can directly see that the field in the through-port appears as the sum of the complex field from the laser cavity and the nanocavity. The power in the corresponding ports is then calculated as

$$P_{t/x}(t) = 2\varepsilon_0 nc\left|A_{t/x}(t)\right|^2 \tag{13}$$

The time-independent steady-state solution of the equations above allows one to calculate the pump-power dependence of the output power of the Fano laser.

Fig. 8 shows an example of the detuning-dependence of the output power in the through-port and the cross-port. As seen, the output power in the cross-port strongly exceeds that of the through-port power for near-resonant conditions, while the through-port power dominates for off-resonant conditions. The reason is that on resonance the waveguide field and the nanocavity field interfere destructively and the transmission to the through-port is strongly suppressed. On the other hand, the field stored in the nanocavity simply leaks to the cross-port, and the small value of this coupling rate is compensated for by the strong enhancement of the nanocavity field at resonance (see example simulation in Fig. 5). For oscillation at the nanocavity resonance and in the absence of a partially transmitting element in the waveguide, one can derive the following approximate expressions for the output power in the through-port ($j = t$) and the cross-port ($j = x$)

$$P_j = \eta_0\eta_j(J - J_{th}); \quad \eta_0 = \frac{\hbar\omega_s}{e}\frac{\Gamma g_s - \alpha_i}{\Gamma g_s} \tag{14}$$

$$\eta_t = \frac{Q}{2Q_i}, \quad \eta_x = \frac{Q_v}{Q_v + 2Q_p} \tag{15}$$

Here, J is the current and it was assumed that the reflectivity of the left mirror is unity and Q_v, $Q_p \gg Q$. We see that for $Q \ll Q_i$ the through-port quantum efficiency is very small while for $Q_v \gg Q_p$, the cross-port efficiency is only limited by the internal losses.

C. *Self-Pulsing – Passive Pulse Generation*

In the case where the nanocavity contains un-pumped active material, it is found that the laser under certain conditions may emit a periodic train of short optical pulses, rather than a continuous-wave field [9]. Fig. 9 shows a phase diagram calculated using the dynamical model presented above with the addition of a rate equation for the carrier density in the nanocavity to represent the active material extending over the entire sample [9], [44]. In the phase diagram, the grey region represents the laser being in a below-threshold state, while the light blue region represents continuous-wave lasing and the yellow region represents a periodic pulse train, as indicated by the insets, which show the temporal evolution of the output power for different parameter values.

The time-periodic steady-state (limit-cycle solution), where a train of short pulses is emitted by the laser, arises due to the nanocavity functioning as a saturable absorber mirror, which leads to passive Q-switching [9]. Due to the active material in the nanocavity, the reflectivity of the Fano mirror becomes saturable, which means that a transient increase in intensity (e.g., from spontaneous emission) will increase the reflectivity by saturating the absorption of the nanocavity further. This reflectivity increase in turn means that the laser field can grow, leading to

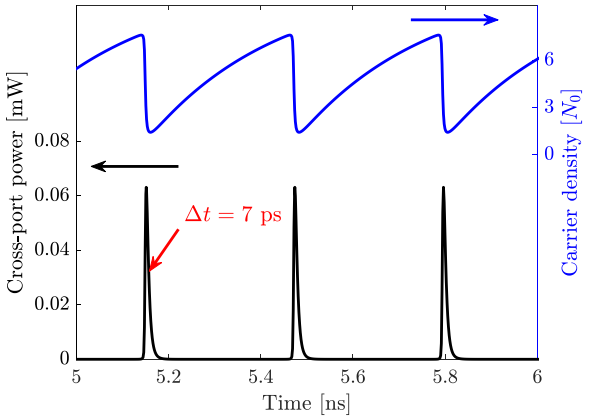

Fig. 10. Cross-port output power and laser-cavity carrier density as functions of time in the self-pulsing state, showing typical Q-switching dynamics.

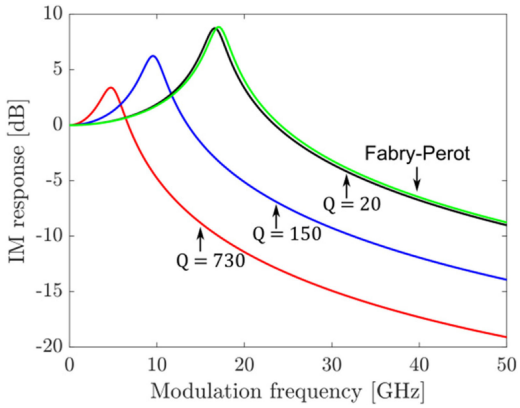

Fig. 11. Intensity modulation response as function of the modulation frequency for a conventional Fabry-Pérot laser (green) and Fano lasers with different values of the nanocavity quality factor (red, blue, black).

further saturation of the absorption, reflectivity increase and further field increase. Eventually this positive feedback loop will deplete the carrier density, resulting in an off-period, while the gain builds back up and the process restarts. In this way, a dynamical equilibrium is established and a stable pulse train is emitted, typically with repetition rates in the few-GHz range and pulsewidths on the order of 10 ps [44]. This is similar to the situation which may be encountered e.g., in VCSELs with an external mirror that includes a an absorbing semiconductor layer that saturates for increasing intensity [52].

Fig. 10 shows an example of the self-pulsing laser dynamics as simulated using the laser model presented in [44]. From Fig. 9 it is clear that a well-defined self-pulsing regime exists. As the bias is increased, the laser eventually transitions from self-pulsing to a CW state, because the continuous-wave power becomes large enough to saturate the mirror reflectivity, such that saturable gain becomes dominant. As the frequency is detuned, the difference between the saturated and unsaturated reflection coefficients decreases, leading to a smaller self-pulsing range. Finally, one must also consider the phase condition, which changes with both the mirror phase and reflectivity through the linewidth enhancement factor, giving rise to the complex shape of the self-pulsing regime. In [44] it was demonstrated how the extent and shape of the self-pulsing regime depends on several laser parameters, such as mirror reflectivity, carrier lifetime in the nanocavity and linewidth enhancement factor.

One can estimate the boundary of the self-pulsing regime by employing a small-signal analysis to determine the stability properties of the system. This type of analysis shows that upon crossing the boundary from the blue region to the yellow region, the laser steady-state solution becomes unstable by way of a complex conjugate pair of eigenvalues, with imaginary parts corresponding to the relaxation oscillation frequency, acquiring positive real parts, corresponding to exponential growth. This is a Hopf bifurcation leading to a periodic solution at the relaxation oscillation frequency. While the temporal variation is near-sinusoidal right after crossing the boundary, the solution quickly acquires higher-order frequency components, corresponding to the generation of a train of short optical pulses. The dashed black line in Fig. 9 represents the stability boundary found from this analysis. The difference between the boundary of the yellow region and the dashed stability boundary is attributed to the occurrence of another bifurcation, a so-called generalized Hopf bifurcation, which gives rise to the coexistence of a stable fixed point solution and a stable limit-cycle solution [53].

D. Ultra-high Speed Modulation

We now consider active modulation of the Fano laser. Conventionally, laser diodes are modulated via the bias current, which controls the gain of the laser via the injected carrier density [2]. As is well-known, the effective lifetime of the carriers (enhanced by stimulated emission) limits the maximum frequency at which the laser output intensity can be efficiently modulated to values close to the relaxation oscillation frequency [2]. For the best lasers today, this value is of the order of 40 GHz. Furthermore, the appearance of a characteristic resonance frequency itself leads to unwanted distortion. If the Fano laser is modulated via the bias current, one observes the same qualitative behavior as for conventional lasers [54], but with different relaxation frequency and damping [46], as demonstrated in Fig. 11. This figure shows the intensity modulation (IM) response as a function of the modulation frequency for Fano lasers (red, blue, black) with different values of the nanocavity quality factor (but same reflectivity) and the corresponding response for a conventional Fabry-Pérot (FP) laser with the same mirror reflectivities (green). It is clear that the shape of the response is the same, but that the Fano laser IM response shows a reduction of the relaxation oscillation resonance frequency as well as the 3 dB-bandwidth. The frequency reduction is seen to scale with the quality factor of the nanocavity, which, as shown previously, corresponds to the bandwidth of the Fano mirror.

The physical origin of the damping is that the Fano mirror functions as a narrowband filter around the lasing wavelength, with a filter bandwidth inversely proportional to the quality factor of the nanocavity. As such, the response also changes depending on the frequency detuning. In the time domain, one can

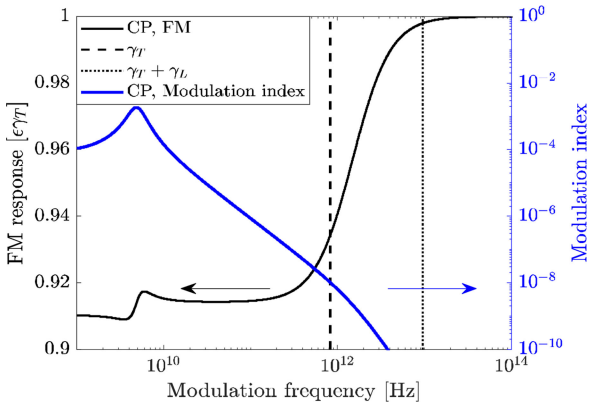

Fig. 12. FM response (black) and modulation index (blue) when modulating the nanocavity resonance frequency. The modulation produces an almost pure FM signal with ultra-large bandwidth.

interpret the nanocavity storage time as an additional delay in the system, reducing the bandwidth [46]. This additional damping is of interest with respect to increasing the feedback stability of lasers, since damping has been shown to increase the critical feedback level at which feedback leads to instabilities and chaos [55], [56]. This is an important property for lasers used as sources for on-chip optical transmission, where optical isolators are impractical, and therefore prompts further investigations of the feedback properties of Fano lasers.

In addition to the conventional intensity modulation, however, Fano lasers have the unique property that they can instead be modulated via the Fano mirror through control of the nanocavity resonance frequency. The underlying physics of this modulation process can be understood as such: A modulation of the refractive index in the nanocavity, using optical or electrical means, results in an instantaneous change of the nanocavity resonance frequency. As discussed previously, the phase of the Fano mirror depends strongly on the detuning between the laser frequency and the nanocavity resonance frequency, meaning that when the resonance frequency is modulated, the laser has to tune its own frequency in order to uphold the phase condition. Depending on the amplitude of this resonance modulation relative to the bandwidth of the Fano mirror, this self-tuning process can result in the generation of an FM signal, which tracks the modulation of the nanocavity resonance frequency directly, or in the generation of a periodic pulse train akin to active Q-switching. In general, there is a gradual transition from an almost pure FM signal for small modulation amplitudes operating near zero detuning, to an FM/IM signal and eventually into the Q-switching regime [8].

When operating in the small-signal regime, the Fano laser displays remarkable properties, as demonstrated in Fig. 12, which shows the FM response (left axis) and corresponding modulation index (right axis) for the field in the cross-port. The FM response is defined as the maximum excursion of the optical frequency, normalized to the modulation amplitude $\epsilon\gamma_T$, while the modulation index is defined as the maximum power amplitude normalized to the steady-state power output.

Two distinct regimes can be identified: For low modulation frequencies, the laser adiabatically tracks the oscillation condition solution except for a resonance at the relaxation oscillation frequency, which is induced by the small amplitude modulation [46]. This resonance exists even for vanishing linewidth enhancement factor, $\alpha = 0$, because the amplitude and phase of the laser are coupled through the dispersive mirror, but vanishes as the detuning approaches zero. The adiabatic tracking occurs because the decay time of the nanocavity field (γ_T) and the roundtrip time of the laser cavity field (γ_L) are both faster than the modulation period. The upper limit of this regime is given by the smaller value of γ_T and γ_L, and as such the conventional behavior of the slowest time constant limiting the conventional modulation bandwidth is also evident here. However, instead of dropping off beyond this limit, the response increases gradually to unity, i.e., the output field exactly tracks the modulation. Unit response is obtained when $\omega_M \gg \gamma_L + \gamma_T$. Above this limit, the modulation is too fast for either field to change appreciably within a cycle (which is why the modulation index goes to zero), meaning that the laser oscillation condition is fulfilled on average, while the nanocavity wavelength responds instantaneously to the modulation through the adiabatic wavelength conversion effect [57]. This essentially corresponds to modulating the nanocavity independently and maintaining the output power through the L-cavity recycling the leaked nanocavity field. As such, the upper limit of this process is given by the limits to the adiabatic wavelength conversion process, which has been numerically demonstrated to be as fast as a few femtoseconds [30]. The parameter region $\min(\gamma_T, \gamma_L) < \omega_m < \gamma_T + \gamma_L$ represents a transition between these two operation regimes, which explains the gradual decrease in modulation index and increase in FM response.

If the modulation amplitude of the nanocavity refractive index is increased such that the corresponding variation of the nanocavity resonance frequency becomes comparable to the Fano mirror linewidth (γ_T), the laser instead enters a complicated Q-switching regime, where microwave power oscillations [8], periodic trains of few-picosecond pulses and chaotic states are all obtainable. Because of the strong asymmetry in the tuning characteristics (Fig. 7) induced by the non-zero linewidth enhancement factor and antisymmetric mirror phase, this wide range of operation states becomes available. In particular, the very abrupt change in threshold gain for negative detuning can lead to short pulses with large peak power, but typically accompanied by some asymmetry in the temporal signal [8], i.e., smaller trailing pulses.

IV. Fabrication of Fano Lasers

A. Device Design

As illustrated in Fig. 6, the quality factor of the lasing mode of the Fano laser depends very sensitively on the geometry of the device and it is therefore of utmost importance to realize a robust design of the Fano laser. As starting point, we take for example a PhC structure having a hexagonal lattice of holes with lattice constant $a = 464$ nm and hole radius $R = 109$ nm, cf. Fig. 13. We focus on the H0-type nanocavity. The first step is to create a resonant mode at a wavelength close to the gain peak of the active material (quantum dots in our case) and to optimize its intrinsic Q-factor. By shifting the two neighboring air

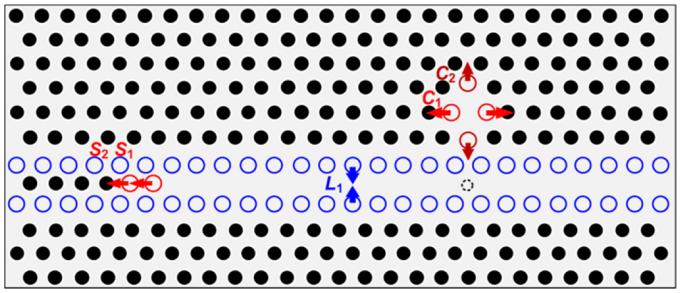

Fig. 13. Example of actual design of a Fano laser indicating the airholes whose positions are changed in order to optimize the quality factor of the laser cavity as well as matching the resonance frequency to the gain spectrum of the quantum dots.

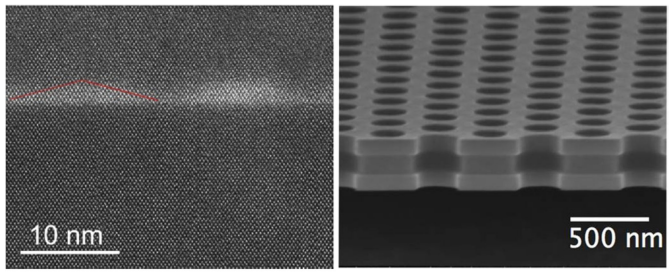

Fig. 14. (a) HAADF STEM microphotograph of a layer of 1.65 ML InAs quantum dots in InP taken in cross-section geometry. The shape of the QD to the left is indicated by red guide lines (b) Example of fabricated membrane structure with embedded active layers, in this case quantum wells.

holes $C_1 = 0.163a$ of the H0 nanocavity in opposite directions horizontally and two other neighboring air holes $C_2 = 0.166a$ in opposite directions vertically, we achieve a nanocavity mode with a calculated intrinsic Q-factor on the order of 3×10^5. Further improvement of the Q-factor can be achieved by shifting or changing the sizes of additional air holes around the nanocavity [58]. Next, we side-couple the optimized H0 nanocavity with a standard W1-type (defined by removing a single row of air holes) open waveguide (WG) and shift the two innermost arrays of holes adjacent to the WG towards the WG center by $L_1 = 0.16a$ to control the cavity-waveguide coupling and realize a total Q-factor of the nanocavity to ∼900, so that the localized mode in the nanocavity can be efficiently coupled with the WG continuum mode (usually in the fast light regime). After that, we block the left part of the WG by air holes, leading to a broadband left mirror. A number of missing holes (e.g., 12) in the WG between the left mirror and the center of the H0 nanocavity forms the laser cavity. We then slightly tune $L_1 = 0.17a$ and shift the outermost air holes (two here) $S_1 = 0.334a$, $S_2 = 0.19a$ at the left mirror to both tune the round trip phase of the light in the WG as well as to minimize the light scattering loss at the left mirror, in order to obtain near-perfect destructive interference for transmission to the waveguide through-port. After optimization, light originally in the continuum mode gets trapped between the left mirror and the nanocavity (Fano mirror), eventually forming a bound state in the continuum, i.e., a composite mode with resonant wavelength close to that of the original H0 nanocavity mode and a Q-factor on the order of 2×10^5. We notice that this Q-factor can be further improved through more advanced (and complicated) hole shifting optimization.

In addition, in order to control the interference condition of the Fano mirror, a blockade hole (see the dashed circle in Fig. 13) can be added in the WG below the nanocavity, as previously discussed. This will make the reflection spectrum of the Fano mirror asymmetric in frequency, which could be used for enhancing the sensitivity of the Fano mirror reflectivity (amplitude and phase) towards modulation of the nanocavity resonance frequency.

B. Processing and Epitaxy

The samples are fabricated on a 250 nm thick InP membrane which contains 3 layers of InAs quantum dots with effective thickness of 1.65 monolayers, separated by 30 nm thick spacers of InP. The photoluminescence spectrum of the InP wafer with quantum dots is centered at 1558 nm with a full width at half maximum of ∼166 nm. The InP structure with a 1 μm silicon dioxide layer is bonded to a silicon carrier using Bisbenzocyclobutene.

Electron beam lithography is used to write the PhC pattern on a positive e-beam resist (ZEP-520A) layer. A ∼200 nm thick SiN_x layer deposited by PECVD is used as a hard mask [59]. After the exposure, the resist is developed and the mask is transferred to the nitride layer through reactive ion etching (RIE). The resist is then removed in a heated ultrasonic bath. After that, the PhC pattern is transferred to the InP layer through an RIE dry etching process and the sample is immersed in a BHF solution with a wetting agent to obtain an air suspended membrane and, at the same time, to remove the SiN_x. More details on the fabrication process can be found in [60].

Concerning the epitaxial details, all samples were grown in a low-pressure (60 Torr) Turbodiscs metal-organic vapor phase epitaxy (MOVPE) reactor on InP (001) substrates in hydrogen ambient with trimethylindium and trimethylgallium as group III precursors, and arsine, phosphine, and tertiarybutylphosphine as group V precursors. The 250 nm InP layer with quantum dots forming the photonic crystal membrane in the final device was deposited on top of a 250 nm sacrificial $In_{0.53}Ga_{0.47}As$ layer at 610 °C. For the QD deposition, the growth temperature was reduced to 485 °C and an InAs layer with effective thickness of 1.65 ML was deposited followed by 10 nm of InP also grown at 485 °C prior to rising the growth temperature back to 610 °C. The resulting QDs are formed on top of a 2 ML InAs wetting layer and have a hexagonal base pyramidal shape with 2.7±0.3 nm height and base diameters of 18.8±5.2 nm and 13.2±1.6 nm in [−1–10] and [−110] crystallographic directions, respectively. High-angle angular dark-field scanning transmission electron microcopy (HAADF STEM) was used to analyze the morphology of the resulting QDs [61]. The image of a QD array in cross-section geometry presented in Fig. 14(a) shows a typical InAs QD layer in the InP matrix. The QD surface density per layer is about $4{\cdot}10\ cm^{-2}$.

V. Experimental Results

A. Experimental Set-Up

The experimental set-up used for characterizing the Fano lasers is shown in Fig. 15.

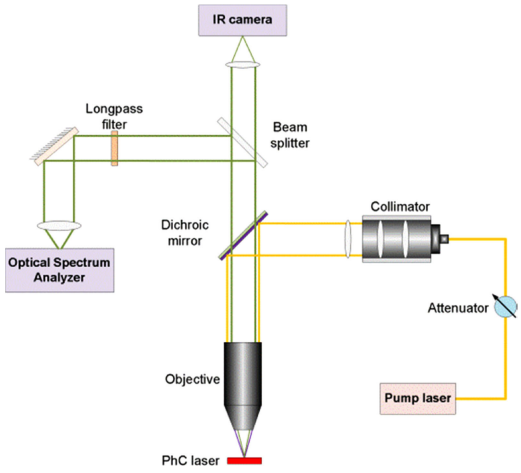

Fig. 15. Experimental set-up for room-temperature characterization of Fano lasers. The lasers are vertically pumped through a microscope objective focused in the laser cavity region by a 1480 nm CW pump laser. Vertically scattered laser light is detected through the same objective.

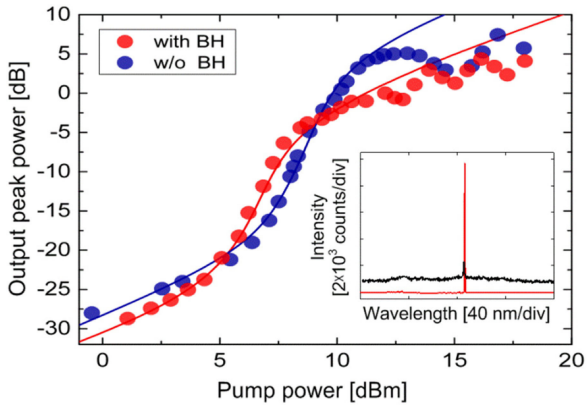

Fig. 16. Measured output power versus pump power. Dots: experimental data; lines: theoretical fit using conventional rate equation model. The red and blue curves correspond to structures with and without a blocking hole (BH) acting as PTE. Inset: optical spectra of the structure with the BH for pump powers of 3 dBm (black) and 7.5 dBm (red). For clarity, the black curve is shifted vertically and the spectrometer integration time is 12 times larger than for the red curve. The cavity length was 12 missing holes.

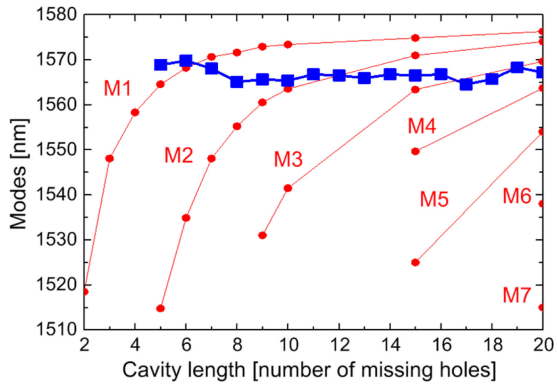

Fig. 17. Measured emission wavelengths versus cavity length for Fano lasers (blue square markers) and ordinary photonic-crystal line-defect cavity lasers (red circular markers). M1–M7 denote the mode order, where M1 is the fundamental mode. Adapted from [9].

The laser samples are vertically pumped with a 1480 nm laser diode using a micro-photoluminescence set-up [60] with precise control of pump position and area, and monitored by an infra-red camera. The full width at half maximum (diameter) of the pump spot is fixed at ∼3 μm. For on-chip applications of the Fano laser, output emission will be via the cross-port or through-port depicted in Fig. 3. However, for the current generation of devices, where active material is present in the entire membrane, these waveguides will absorb the emitted light since the active material in those waveguides is un-pumped. Experimentally, the emission from the Fano laser is therefore collected vertically using the same objective lens as for pumping, having a numerical aperture of 0.65. The transmission efficiency from the pump diode to the objective is ∼30% and the vertical collection efficiency is ∼20% (estimated by comparing the farfield pattern of the laser emission with the lens numerical aperture), which may vary slightly for different cavity structures. All measurements are performed with continuous-wave injection at room temperature. For the output spectral measurements, after being isolated from the reflected pump beam by a long-pass filter, the signal is analyzed using an optical spectrum analyzer, or a highly sensitive spectrometer with a cooled low-noise InGaAs one-dimensional detector array. For the radio frequency measurements, the collected output signal is first amplified using a low-power erbium doped fiber amplifier cascaded with a tunable optical band-pass filter followed by an optical isolator, after which the signal is re-amplified using a standard in-line erbium doped fiber amplifier, filtered using another tunable optical band-pass filter, and detected with a photodiode and monitored with a radio frequency spectrum analyzer having a bandwidth of 22 GHz. For the optical and radio frequency spectrum measurements, the spectral scan speed was chosen as a good compromise between the need to obtain a sufficiently high signal-to-noise ratio, and the requirement to minimize thermal drift.

B. CW Operation

Fig. 16 shows the measured output power from a Fano laser as a function of the optical pump power. A clear transition to lasing is seen, in accordance with the optical spectrum shown as an insert. A single dominant mode at 1,566 nm is observed. For high pump powers, the output peak power is found to fluctuate with the input pump power. We ascribe this to two main factors. Firstly, the mode becomes unstable at high pump powers due to optical nonlinearities, as will be discussed later. Secondly, thermal effects become more important at high pump power levels, degrading the lasing performance due to reduced material gain as well as changes in the refractive index. The latter may lead to a decrease of the Q-factor of the laser cavity mode, considering the sensitive dependence of that mode on device parameters, cf. Fig. 6.

In order to demonstrate that the lasing wavelength of the Fano laser is pinned by the nanocavity frequency, Fig. 17 shows the measured lasing wavelengths versus cavity length for Fano lasers

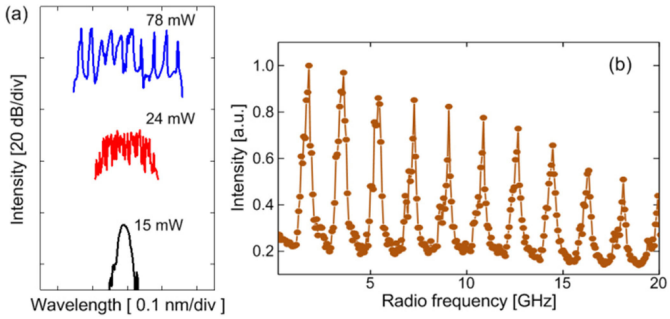

Fig. 18. (a) Measured optical spectra of the Fano laser for pump powers of 15, 24, and 78 mW. For clarity, the spectra are shifted vertically. (b) Measured RF spectrum of the laser power for a pump power of 60 mW.

[9] and ordinary PhC line-defect lasers with both left and right mirrors being composed of a terminated waveguide [62], as a comparison. The Fano lasers were found to be single-mode with a wavelength that is nearly independent of the cavity length. This is in stark contrast to ordinary PhC lasers with a line-defect cavity, where several longitudinal modes are observed, and where all the modes shift to longer wavelengths with increasing cavity length, consistent with the modes approaching the PhC Brillouin zone edge [62]; see the red lines in Fig. 17. This demonstrates the unique mode selection properties of Fano lasers enabled by the narrowband mirror. Furthermore, the pinning of the laser wavelength by the nanocavity resonance avoids the transition into the slow-light region with increasing laser length, which was shown to lead to an unconventional increase in laser threshold with cavity length [62].

C. Self-Pulsing

While the Fano laser spectrum typically narrows as the pump power is increased, for some lasers we observe a broadening of the optical spectrum above threshold, accompanied by the development of a series of equidistant peaks in the spectrum of the photocurrent (radio-frequency spectrum). This is illustrated in Fig. 18. These features strongly suggest that the laser undergoes a transition from CW lasing to the generation of a self-sustained train of short pulses, which is supported by dynamical simulations of our developed Fano laser model. The highest measured repetition frequency is $\sim$8 GHz, obtained for the laser without a blockade hole. The self-pulsation in the laser without a blockade hole is quenched when the pump power exceeds 60 mW. Simulations show that pulses with width down to 15 ps and peak power of $\sim$1.2 mW (propagating in the WG direction) are achieved for the laser containing a blockade hole.

The physical mechanism of self-pulsing is similar to the case of a semiconductor-saturable mirror leading to passive Q-switching of external cavity lasers [34]. However, the extreme miniaturization enabled by our configuration as well as the Fano resonance adds additional richness and design opportunities. Compared to the theoretical suggestion of coupled-cavity structures for realizing self-pulsing [63], the Fano laser demonstrated here relies on the coupling of a very low Q-factor cavity (semi-open waveguide) and a cavity with much higher Q-factor (the nanocavity), leading to single-mode operation rather than a mode doublet.

VI. Conclusion and Outlook

We have described the basic physical properties of a new type of laser with a mirror based on Fano interference [8]. It is a characteristic feature of the Fano laser that one (or both) of the mirrors has a narrow-band reflection spectrum, determined by the properties of a cavity that is side-coupled to the laser waveguide. In combination with the phase condition of the laser cavity this leads to a very sensitive dependence of the laser on the tuning of the resonance, similar to the situation of lasers based on a bound mode in the continuum, implying that the laser can be efficiently modulated via the mirror. It was theoretically demonstrated that this should allow modulation of the laser at frequencies far beyond the relaxation oscillation resonance limiting conventional lasers.

The Fano laser has been experimentally demonstrated using a photonic crystal membrane structure with quantum dot active material [9]. The Fano lasers investigated so far were optically pumped, but can be electrically biased using schemes similar to that developed in [5]. The Fano laser was found under some conditions to undergo a transition to self-Q switching, leading to the generation of a train of short optical pulses with repetition rates in the gigahertz regime [9]. The self-pulsing behavior is well-explained by a dynamical model developed for the Fano laser and originates from nonlinearities in the Fano mirror due to absorption saturation.

The Fano laser geometry opens for a number of promising research directions. By modulating the laser via the nanocavity, the modulation response will not be limited by the intrinsic relaxation oscillation frequency, but rather by the speed and amplitude of the nanocavity resonance. This avenue thus demands research into effective nanoelectrode geometries. The Fano laser geometry also allows for optical modulation of the nanocavity, which is of interest for exploring the intrinsic frequency response as well as for optical signal processing applications, possibly with transistor-like response.

Preliminary investigations furthermore indicate that the Fano laser is very robust towards optical feedback, which leads to instabilities and chaotic dynamics for conventional lasers. The Fano laser geometry may therefore be very attractive for on-chip applications since back-reflections are common but it is difficult to implement an isolator.

Due to the rich dynamics of Fano lasers, the many design opportunities, and the possibilities for realizing new electrical and optical control schemes via modulation of the nanocavity, we believe that further research on Fano lasers is warranted.

Acknowledgment

The authors would like to acknowledge helpful discussions with M. Heuck, W. Xue, L. Ottaviano, and Y. Chen. The authors would also like to thank S. Kadkhodazadeh, DTU Nanolab, for providing STEM characterization of the quantum dots.

REFERENCES

[1] D. A. B. Miller, "Attojoule optoelectronics for low-energy information processing and communications," *J. Lightw. Technol.*, vol. 35, no. 3, pp. 346–396, Feb. 2017.

[2] L. A. Coldren, S. W. Corzine, and M. L. Masanovic, *Diode Lasers and Photonic Integrated Circuits*, 2nd ed. Hoboken, NJ, USA: Wiley, 2012.

[3] O. Painter *et al.*, "Two-dimensional photonic band-gap defect mode laser," *Science*., vol. 284, no. 5421, pp. 1819–1821, Jun. 1999.

[4] Y. Akahane, T. Asano, B. Song, and S. Noda, "High-Q photonic nanocavity in a two-dimensional photonic crystal," *Nature*, vol. 425, pp. 944–947, 2003.

[5] S. Matsuo *et al*., "Ultralow operating energy electrically driven photonic crystal lasers," *IEEE J. Sel. Topics Quantum Electron.*, vol. 19, no. 4, Jul. 2013, Art. no. 4900311.

[6] S. L. McCall, A. F. J. Levi, R. E. Slusher, S. J. Pearton, and R. A. Logan, "Whispering-gallery mode microdisk lasers," *Appl. Phys. Lett.*, vol. 60, no. 3, pp. 289–291, 1992.

[7] H. Cao *et al*., "Spatial confinement of laser light in active random media," *Phys. Rev. Lett.*, vol. 84, no. 24, pp. 5584–5587, 2000.

[8] J. Mork, Y. Chen, and M. Heuck, "Photonic crystal fano laser: Terahertz modulation and ultrashort pulse generation," *Phys. Rev. Lett.*, vol. 113, no. 16, Oct. 2014, Art. no. 163901.

[9] Y. Yu, W. Xue, E. Semenova, K. Yvind, and J. Mork, "Demonstration of a self-pulsing photonic crystal Fano laser," *Nature Photon.*, vol. 11, no. 2, pp. 81–84, Dec. 2017.

[10] A. E. Miroshnichenko, S. Flach, and Y. S. Kivshar, "Fano resonances in nanoscale structures," *Rev. Mod. Phys.*, vol. 82, no. 3, pp. 2257–2298, 2010.

[11] M. F. Limonov, M. V Rybin, A. N. Poddubny, and Y. S. Kivshar, "Fano resonances in photonics," *Nature Photon.*, vol. 11, no. 9, pp. 543–554, Sep. 2017.

[12] M. V. Rybin *et al*., "Purcell effect and Lamb shift as interference phenomena," *Sci. Rep.*, vol. 6, 2016, Art. no. 20599.

[13] C. W. Hsu, B. Zhen, A. D. Stone, J. D. Joannopoulos, and M. Soljačić, "Bound states in the continuum," *Nature Rev. Mater.*, vol. 1, no. 9, Jul. 2016, Art. no. 16048.

[14] A. Kodigala, T. Lepetit, Q. Gu, B. Bahari, Y. Fainman, and B. Kanté, "Lasing action from photonic bound states in continuum," *Nature*, vol. 541, no. 7636, pp. 196–199, 2017.

[15] M. Rybin and Y. Kivshar, "Supercavity lasing inflation identified," *Nature*, vol. 541, pp. 164–165, 2017.

[16] S. Johnson, P. Villeneuve, S. Fan, and J. Joannopoulos, "Linear waveguides in photonic-crystal slabs," *Phys. Rev. B*, vol. 62, no. 12, pp. 8212–8222, Sep. 2000.

[17] G. Crosnier *et al*., "Hybrid indium phosphide-on-silicon nanolaser diode," *Nature Photon.*, vol. 11, no. 5, pp. 297–300, 2017.

[18] B. E. Little, S. T. Chu, H. A. Haus, J. Foresi, and J. Laine, "Microring resonator channel dropping filters," *J. Lightw. Technol.*, vol. 15, no. 6, pp. 998–1005, Jul. 1997.

[19] K. Nozaki, A. Shinya, S. Matsuo, T. Sato, E. Kuramochi, and M. Notomi, "Ultralow-energy and high-contrast all-opticalswitch involving Fano resonance based on coupled photonic crystal nanocavities," *Opt. Express*, vol. 21, no. 10, pp. 3069–3071, 2013.

[20] M. Heuck, P. T. Kristensen, Y. Elesin, and J. Mork, "Improved switching using Fano resonances in photonic crystal structures," *Opt. Lett.*, vol. 38, no. 14, pp. 2466–2468, Jul. 2013.

[21] Y. Yu *et al*., "Fano resonance control in a photonic crystal structure and its application to ultrafast switching," *Appl. Phys. Lett.*, vol. 105, no. 6, Aug. 2014, Art. no. 061117.

[22] G. Dong, Y. Wang, and X. Zhang, "High-contrast and low-power all-optical switch using Fano resonance based on a silicon nanobeam cavity," *Opt. Lett.*, vol. 43, pp. 5977–5980, 2018.

[23] J. Zhang *et al*., "Generating Fano resonances in a single-waveguide silicon nanobeam cavity for efficient electro-optical modulation," *ACS Photon.*, vol. 5, no. 11, pp. 4229–4237, Nov. 2018.

[24] D. Bekele *et al*., "Signal reshaping and noise suppression using photonic crystal Fano structures," *Opt. Express*, vol. 26, pp. 19596–19605, 2018.

[25] W. Zhou *et al*., "Progress in 2D photonic crystal Fano resonance photonics," *Prog. Quantum Electron.*, vol. 38, no. 1, pp. 1–74, Jan. 2014.

[26] C. J. Chang-Hasnain and W. Yang, "High-contrast gratings for integrated optoelectronics," *Adv. Opt. Photon.*, vol. 4, no. 3, pp. 379–440, Sep. 2012.

[27] G. C. Park *et al*., "Hybrid vertical-cavity laser with lateral emission into a silicon waveguide," *Laser Photon. Rev*., vol. 9, no. 3, pp. 11–15, 2015.

[28] U. Fano, "Effect of configuration interaction on intensities and phase shifts," *Physical Rev.*, vol. 124, no. 6, pp. 1866–1878, 1961.

[29] S. Fan, "Sharp asymmetric line shapes in side-coupled waveguide-cavity systems," *Appl. Phys. Lett.*, vol. 80, no. 6, pp. 908–910, 2002.

[30] M. Notomi, "Manipulating light with strongly modulated photonic crystals," *Rep. Prog. Phys.*, vol. 73, no. 9, Sep. 2010, Art. no. 096501.

[31] S.-H. Kim and Y.-H. Lee, "Symmetry relations of two-dimensional photonic crystal cavity modes," *IEEE J. Quantum Electron.*, vol. 39, no. 9, pp. 1081–1085, Sep. 2003.

[32] Z. Zhang and M. Qiu, "Small-volume waveguide-section high Q microcavities in 2D photonic crystal slab," *Opt. Express*, vol. 12, no. 17, pp. 3988–3995, Aug. 2004.

[33] K. Nozaki *et al*., "Sub-femtojoule all-optical switching using a photonic-crystal nanocavity," *Nature Photon.*, vol. 4, no. 7, pp. 477–483, Jul. 2010.

[34] H. Choi, M. Heuck, and D. Englund, "Self-similar nanocavity design with ultrasmall mode volume for single-photon nonlinearities," *Phys. Rev. Lett.*, vol. 118, no. 22, May 2017, Art. no. 223605.

[35] S. Hu *et al*., "Experimental realization of deep-subwavelength confinement in dielectric optical resonators," *Sci. Adv.*, vol. 4, no. 8, Aug. 2018, Art. no. eaat2355.

[36] F. Wang, R. E. Christiansen, Y. Yu, J. Mørk, and O. Sigmund, "Maximizing the quality factor to mode volume ratio for ultra-small photonic crystal cavities," *Appl. Phys. Lett.*, vol. 113, no. 24, Dec. 2018, Art. no. 241101.

[37] P. T. Kristensen, J. R. de Lasson, M. Heuck, N. Gregersen, and J. Mork, "On the theory of coupled modes in optical cavity-waveguide structures," *J. Lightw. Technol.*, vol. 35, no. 19, pp. 4247—4259, Oct. 2017.

[38] Y. Yu *et al*., "Nonreciprocal transmission in a nonlinear photonic-crystal Fano structure with broken symmetry," *Laser Photon. Rev.*, vol. 9, no. 2, pp. 241–247, 2015.

[39] A. D. Osterkryger *et al.*, "Spectral symmetry of Fano resonances in a waveguide coupled to a microcavity," *Opt. Lett.*, vol. 41, no. 9, p. 2065, May 2016.

[40] K. Nozaki *et al.*, "Ultralow-energy and high-contrast all-optical switch involving Fano resonance based on coupled photonic crystal nanocavities," *Opt. Express*, vol. 21, no. 10, pp. 11877–11888, May 2013.

[41] Y. Yu, H. Hu, L. K. Oxenløwe, K. Yvind, and J. Mork, "Ultrafast all-optical modulation using a photonic-crystal Fano structure with broken symmetry," *Opt. Lett.*, vol. 40, no. 10, pp. 2357–2360, May 2015.

[42] D. A. Bekele *et al*., "Pulse carving using nanocavity-enhanced nonlinear effects in photonic crystal Fano structures," *Opt. Lett.*, vol. 43, no. 4, pp. 955–958, Feb. 2018.

[43] H. Sekoguchi, Y. Takahashi, T. Asano, and S. Noda, "Photonic crystal nanocavity with a Q-factor of ∼9 million," *Opt. Express*, vol. 22, no. 1, pp. 916–924, 2014.

[44] T. S. Rasmussen, Y. Yu, and J. Mork, "Theory of self-pulsing in photonic crystal Fano lasers," *Laser Photon. Rev.*, vol. 11, no. 5, Sep. 2017, Art. no. 1700089.

[45] P. Lalanne, C. Sauvan, and J. P. Hugonin, "Photon confinement in photonic crystal nanocavities," *Laser Photon. Rev*., vol. 2, no. 6, pp. 514–526, Dec. 2008.

[46] T. S. Rasmussen, Y. Yu, and J. Mork, "Modes, stability, and small-signal response of photonic crystal Fano lasers," *Opt. Express*, vol. 26, no. 13, pp. 16365–16376, Jun. 2018.

[47] P. Hamel *et al*., "Spontaneous mirror-symmetry breaking in coupled photonic-crystal nanolasers," *Nature Photon.*, vol. 9, no. 5, pp. 311–315, 2015.

[48] Y. Tanaka *et al.*, "Dynamic control of the Q factor in a photonic crystal nanocavity," *Nature Mater.*, vol. 6, no. 11, pp. 862–865, 2007.

[49] B. Tromborg, H. Olesen, X. Pan, and S. Saito, "Transmission line description of optical feedback and injection locking for fabry-perot and DFB lasers," *IEEE J. Quantum Electron.*, vol. QE-23, no. 11, pp. 1875–1889, Nov. 1987.

[50] C. Husko, A. De Rossi, S. Combrié, Q. V. Tran, F. Raineri, and C. W. Wong, "Ultrafast all-optical modulation in GaAs photonic crystal cavities," *Appl. Phys. Lett.*, vol. 94, no. 2, Jan. 2009, Art. no. 021111.

[51] Y. Yu *et al*., "Switching characteristics of an InP photonic crystal nanocavity: Experiment and theory," *Opt. Express*, vol. 21, no. 25, pp. 31047–31061, Dec. 2013.

[52] U. Keller and K. Weingarten, "Semiconductor saturable absorber mirrors (SESAM's) for femtosecond to nanosecond pulse generation in solid-state lasers," *IEEE J. Sel. Topics Quantum Electron.*, vol. 2, no. 3, pp. 435–453, Sep. 1996.

[53] P. M. Kaminski, S. Arslanagic, J. Mørk, and J. Li, "A two-dimensional phase-space picture of the photonic crystal Fano laser," *Phys. Rev. A*, submitted for publication.

[54] A. R. Zali, M. K. Moravvej-Farshi, Y. Yu, and J. Mork, "Small and large signal analysis of photonic crystal Fano laser," *J. Lightw. Technol.*, vol. 36, no. 23, pp. 5611–5616, Dec. 2018.
[55] K. Petermann, "External optical feedback phenomena in semiconductor lasers," *IEEE J. Sel. Topics Quantum Electron.*, vol. 1, no. 2, pp. 480–489, Jun. 1995.
[56] J. Mork, B. Tromborg, and J. Mark, "Chaos in semiconductor lasers with optical feedback: theory and experiment," *IEEE J. Quantum Electron.*, vol. 28, no. 1, pp. 93–108, Jan. 1992.
[57] B. A. Daniel, D. N. Maywar, and G. P. Agrawal, "Dynamic mode theory of optical resonators undergoing refractive index changes," *J. Opt. Soc. Amer. B*, vol. 28, no. 9, pp. 2207–2215, Sep. 2011.
[58] T. Nakamura, Y. Takahashi, Y. Tanaka, T. Asano, and S. Noda, "Improvement in the quality factors for photonic crystal nanocavities via visualization of the leaky components," *Opt. Express*, vol. 24, no. 9, pp. 9541–9549, 2016.
[59] M. Schubert *et al.*, "Lambda shifted photonic crystal cavity laser," *Appl. Phys. Lett.*, vol. 97, no. 19, Nov. 2010, Art. no. 191109.
[60] W. Xue *et al.*, "Thermal analysis of line-defect photonic crystal lasers," *Opt. Express*, vol. 23, no. 14, pp. 18277–18287, 2015.
[61] S. Kadkhodazadeh, "High resolution STEM of quantum dots and quantum wires," *Micron*, vol. 44, no. 1, pp. 75–92, 2013.
[62] W. Xue *et al.*, "Threshold characteristics of slow-light photonic crystal lasers," *Phys. Rev. Lett.*, vol. 116, no. 6, Feb. 2016, Art. no. 063901.
[63] A. M. Yacomotti, S. Haddadi, and S. Barbay, "Self-pulsing nanocavity laser," *Phys. Rev. A*, vol. 87, no. 4, Apr. 2013, Art. no. 041804.

Jesper Mork received the M.Sc., Ph.D., and Dr. Techn. degrees from the Technical University of Denmark (DTU), Lyngby, in 1986, 1988, and 2003, respectively. Since 2002, he has been a Professor in semiconductor photonics and since 2008, he has been heading the Nanophotonics Section, DTU Fotonik. He is the author of more than 245 papers in refereed journals and around 350 contributions to international conferences, including more than 90 invited talks. His current research interests include semiconductor quantum photonics, photonic crystal structures, slow light, nano- and microcavity lasers, and integrated photonics. He is a Fellow of OSA and is an Associate Editor for *Optica*.

Yi Yu received the B.Sc. and M.Eng. degrees from the Huazhong University of Science and Technology, Wuhan, China, in 2008 and 2011, respectively, and the Ph.D. degree from the Technical University of Denmark (DTU), Kongens Lyngby, Denmark, in 2015. Since then, he has been a Postdoc with DTU Fotonik and is currently with the Institute of Physics, Ecole Polytechnique Federale de Lausanne, Lausanne, Switzerland. His current research focuses on nanocavity lasers and quantum nanophotonic structures.

Thorsten S. Rasmussen received the M.Sc. degree in photonics engineering in 2017 from the Technical University of Denmark, Kongens Lyngby, Denmark, where he is currently working toward the Ph.D. degree. He is the first author of two papers in refereed journals, as well as seven contributions to international research conferences. His research interests include theory and modeling of laser dynamics, photonic crystal structures, Fano lasers, and lasers with optical feedback.

Elizaveta Semenova received the B.Sc. and M.Sc. degrees from St.-Petersburg State Technical University, St.-Petersburg, Russia, in 1999 and 2001, respectively, and the Ph.D. degree in semiconductor physics from A.F. Ioffe Institute, St.-Petersburg, Russia, in 2005. She is currently a Senior Researcher with the Technical University of Denmark, Kongens Lyngby, Denmark. Her research interests are focused on the development and the optimization of the epitaxial growth process of new III-V semiconductor materials for optoelectronic applications, including III-V on Si. She is a co-author of more than 76 peer-reviewed scientific publications.

Kresten Yvind received the M.Sc.E. and Ph.D. degrees in 1999 and 2003, respectively, from the Research Center for Communication, Optics and Materials, Technical University of Denmark, Kongens Lyngby, Denmark. The center was renamed DTU Fotonik in 2008, and he is currently Professor there. His work is centered on III-V and silicon optoelectronic devices and involves design, growth, processing, and high-speed characterization. Membrane-based devices (on silicon) have been a focus in the last decade leading to efficient nonlinear integrated photonics and various (active) photonics crystal devices for optical interconnects.